

# Uniform mesoporous silica coated iron oxide nanoparticles as a highly efficient, nontoxic MRI $T_2$ contrast agent with tunable proton relaxivities

Fei Ye<sup>a\*</sup>, Sophie Laurent<sup>b</sup>, Andrea Fornara<sup>a,c</sup>, Laura Astolfi<sup>d</sup>, Jian Qin<sup>a,e</sup>, Alain Roch<sup>b</sup>, Alessandro Martini<sup>d</sup>, Muhammet S. Toprak<sup>a\*</sup>, Robert N. Muller<sup>b</sup> and Mamoun Muhammed<sup>a</sup>



**ABSTRACT:** Monodisperse mesoporous silica (mSiO<sub>2</sub>) coated superparamagnetic iron oxide (Fe<sub>3</sub>O<sub>4</sub>@mSiO<sub>2</sub>) nanoparticles (NPs) have been developed as a potential magnetic resonance imaging (MRI)  $T_2$  contrast agent. To evaluate the effect of surface coating on MRI contrast efficiency, we examined the proton relaxivities of Fe<sub>3</sub>O<sub>4</sub>@mSiO<sub>2</sub> NPs with different coating thicknesses. It was found that the mSiO<sub>2</sub> coating has a significant impact on the efficiency of Fe<sub>3</sub>O<sub>4</sub> NPs for MRI contrast enhancement. The efficiency increases with the thickness of mSiO<sub>2</sub> coating and is much higher than that of the commercial contrast agents. Nuclear magnetic resonance (NMR) relaxometry of Fe<sub>3</sub>O<sub>4</sub>@mSiO<sub>2</sub> further revealed that mSiO<sub>2</sub> coating is partially permeable to water molecules and therefore induces the decrease of longitudinal relaxivity,  $r_1$ . Biocompatibility evaluation of various sized (ca. 35–95 nm) Fe<sub>3</sub>O<sub>4</sub>@mSiO<sub>2</sub> NPs was tested on OC-k3 cells and the result showed that these particles have no negative impact on cell viability. The enhanced MRI efficiency of Fe<sub>3</sub>O<sub>4</sub>@mSiO<sub>2</sub> highlights these core-shell particles as highly efficient  $T_2$  contrast agents with high biocompatibility. Copyright © 2012 John Wiley & Sons, Ltd.

Supporting information may be found in the online version of this paper

**Keywords:** MRI; contrast agent; superparamagnetic; iron oxide; mesoporous silica; coating thickness; tunable relaxivity; biocompatibility

## 1. INTRODUCTION

Contrast-enhanced magnetic resonance imaging (MRI) has emerged as a promising technique for the detection, diagnosis, and staging of tumors and cancer using contrast agents to improve the visibility of the internal structure and accurately characterize different types of lesions (1–3). Magnetic contrast agents in MRI are used to modify the relaxation time of protons in the tissues where they accumulate, which causes changes of MR signal intensity and consequently the imaging contrast (4). Depending on whether the contrast-agent induced shortening of relaxation time is greater for  $T_1$  (longitudinal) or  $T_2$  (transverse) relaxation, MRI contrast agents are described as either ' $T_1$  agents' or ' $T_2$  agents'. Superparamagnetic iron oxide nanoparticles (SPIONs) with various sizes and coating materials have been extensively studied because of their capacity to enhance the proton relaxation under the influence of magnetic fields (5,6). For *in vivo* applications, these magnetic nanoparticles (NPs) are required to be biocompatible, water-dispersible, stable and uniform in size (7,8). Conventional aqueous-phase synthesized iron oxide NPs usually exhibit broad size distribution and need extra surface coatings such as dextran (9), citrate (10) or silane (11) to prevent aggregation. Monodisperse and highly crystalline iron oxide NPs were later produced through nonhydrolytic thermal-decomposition of metal-complex precursors (12,13), but the dispersion in nonpolar organic solvent restricts their

biomedical applications. Several studies have dealt with the improvement of the aqueous stability of these hydrophobic iron oxide NPs, for instance, by ligand exchange with water-soluble molecules (14) or hydrophobic interaction with amphiphilic polymers (15,16). More recently, mesoporous silica (mSiO<sub>2</sub>) was selected as a coating material for various nanocrystals to

\* Correspondence to: Muhammet Toprak and Fei Ye, Functional Materials Division, Royal Institute of Technology (KTH), Electrum 229, 164 40 Kista (Stockholm), Sweden. Email: toprak@kth.se

a F. Ye, A. Fornara, J. Qin, M. S. Toprak, M. Muhammed  
Functional Materials Division, Royal Institute of Technology (KTH), Electrum 229, 164 40 Kista, Stockholm, Sweden

b S. Laurent, A. Roch, R. N. Muller  
NMR and Molecular Imaging Laboratory, Department of General, Organic and Biomedical Chemistry, University of Mons, B-7000 Mons, Belgium

c A. Fornara  
YKI, Institute for Surface Chemistry, Drottning Kristinas väg 45, 114 28 Stockholm, Sweden

d L. Astolfi, A. Martini  
Bioacoustics Research Laboratory, Department of Neuroscience, University of Padua, via G. Orus, 2b, 35129 Padua, Italy

e J. Qin  
ABB Corporate Research, Forskargränd 7, 721 78 Västerås, Sweden

stabilize their aqueous dispersion and alleviate the toxicity (17–19). In addition, mSiO<sub>2</sub> hold great potential in diagnostic and therapeutic applications owing to its unique features of ordered pore network, high surface area, large pore volume and possibilities for further functionalization (20,21).

Several reports have focused on the synthesis and investigation of magnetic and mesoporous nanocomposites with core–shell (17) or hybrid structures (22). In order to achieve high colloidal stability, size-dependent properties and long blood circulation for *in vivo* applications, discrete and uniformly small-sized NPs are desired, so as to escape from phagocytes in the reticuloendothelial system (RES) and circulate with a long blood half-life (23). For magnetic NPs used as an MRI contrast agent, the efficiency for contrast enhancement is assessed in terms of its relaxivities  $r_1$  and  $r_2$ , which indicates the ability of a contrast agent to decrease the relaxation times (5). For a  $T_2$  contrast agent, the higher the  $r_2$  (24) and  $r_2/r_1$  ratio (25), the better the contrast efficacy. The contrast-enhancement property of magnetic materials has been modulated typically by their particle size and is well demonstrated in the case of iron oxide NPs (14,26), where the mass-magnetization values and the relaxivity coefficient  $r_2$  gradually increase as a function of particle size from a few to tens of nanometers. However, there are only a limited number of reports concerning the surface coating effect on magnetic relaxivity by biocompatible polymers (27–29) or silica coatings (30,31). It is important to understand the relationship between the coating properties and the changes in relaxivities for designing magnetic NP probes for MRI, in which a high contrast typically leads to a high sensitivity and reduces the amount of contrast agents required for imaging.

In this study, we synthesized mSiO<sub>2</sub>-coated Fe<sub>3</sub>O<sub>4</sub> (Fe<sub>3</sub>O<sub>4</sub>@mSiO<sub>2</sub>) core–shell NPs via a surfactant templated sol–gel method. Parameters such as reactant concentrations were precisely controlled in order to achieve high quality core–shell NPs with varied particle sizes. These monodisperse Fe<sub>3</sub>O<sub>4</sub>@mSiO<sub>2</sub> NPs with variable shell thicknesses could be an ideal model system to assess the effect of surface coatings on the efficiency of NPs as MRI  $T_2$  contrast agents. Moreover, to understand the effect of mSiO<sub>2</sub> coating on proton relaxation, Fe<sub>3</sub>O<sub>4</sub>@mSiO<sub>2</sub> NPs was examined by nuclear magnetic resonance (NMR) relaxometry. Biocompatibility of Fe<sub>3</sub>O<sub>4</sub>@mSiO<sub>2</sub> NPs with different particle sizes was evaluated on OC-k3 cells, which represent a suitable model for the *in vitro* study of ototoxicity (32). This study offers a gateway for in-depth understanding and control of the contrast-enhancing property when designing a novel MRI contrast agent for cutting edge applications such as molecular imaging, where high-resolution imaging is needed.

## 2. EXPERIMENTAL METHODS

### 2.1. Synthesis of mesoporous silica coated SPIONs

All chemicals were purchased from Sigma-Aldrich and were used without purification. Monodisperse SPIONs were synthesized using a previously reported method via thermal decomposition of Fe–oleate complex in dioctyl ether at ca. 297 °C in the presence of oleic acid (13). The Fe<sub>3</sub>O<sub>4</sub> nanocrystals were stabilized with oleic acid and dispersed in chloroform at a concentration of 7.9 mg Fe ml<sup>−1</sup>. Oleic acid-capped Fe<sub>3</sub>O<sub>4</sub> NPs (0.5 ml) were transferred to water by mixing the particles with aqueous cetyltrimethyl ammonium bromide (CTAB) solution at 65 °C and the mixture was vigorously stirred until all the

chloroform had evaporated. To create an mSiO<sub>2</sub> coating layer on CTAB-capped Fe<sub>3</sub>O<sub>4</sub> (Fe<sub>3</sub>O<sub>4</sub>–CTAB) NPs, the aqueous suspension of Fe<sub>3</sub>O<sub>4</sub> was diluted with water and the pH was adjusted to pH 12 by the addition of NaOH. After the temperature of the reaction solution had reached 70 °C, tetraethyl orthosilicate (TEOS; see details in Table 1) and ethyl acetate (EtOAc) in a 1:4 ratio were slowly added in sequence (17). After 2 h, the Fe<sub>3</sub>O<sub>4</sub>@mSiO<sub>2</sub> core–shell particles were collected by centrifugation and washed with ethanol (EtOH) twice. To extract CTAB from mesopore channels, the particles were redispersed in ethanolic NH<sub>4</sub>NO<sub>3</sub> solution (10 mg ml<sup>−1</sup>) at 60 °C and mixed for 30 min (33).

### 2.2. Characterization

The morphology of Fe<sub>3</sub>O<sub>4</sub>@mSiO<sub>2</sub> NPs was characterized by JEM-2100F field emission transmission electron microscope (TEM) operating at an accelerating voltage of 200 kV. Powder X-ray diffraction (XRD) patterns were recorded on a PANalytical X'Pert Pro powder diffractometer with Cu-K<sub>α</sub> radiation (45 kV, 35 mA). Nitrogen sorption isotherms were obtained on a Micromeritics ASAP 2020 pore analyzer at 77 K under continuous adsorption conditions. The Brunauer–Emmett–Teller (BET) method was used to determine the surface area from adsorption data obtained in the range of relative pressure  $p/p_0 = 0.05$  and 0.3. The total pore volume was calculated from the amount of N<sub>2</sub> adsorbed at  $p/p_0 = 0.98$ . A nonlocal density functional theory (NLDFT) model was applied to determine the pore size distribution (PSD). Fe concentration was measured using a Thermo Scientific iCAP 6500 inductively coupled plasma spectrometer. The magnetization measurements were performed using a vibrating sample magnetometer (VSM-Nuovo Molspin, Newcastle-Upon-Tyne, UK). The hydrodynamic diameter of the particles was measured by photon correlation spectroscopy (Delsa<sup>TM</sup>Nano particle size analyzer, Beckman Coulter). Fourier transform infrared (FTIR) spectra were obtained using a Nicolet iS10 FT-IR spectrometer (Thermo Scientific).

### 2.3. Relaxometry

Aqueous dispersions of Fe<sub>3</sub>O<sub>4</sub>–CTAB and Fe<sub>3</sub>O<sub>4</sub>@mSiO<sub>2</sub> NPs with different shell thicknesses were examined by MR relaxometry.

**Table 1.** Summary of composition of reactants for the synthesis of Fe<sub>3</sub>O<sub>4</sub>@mSiO<sub>2</sub> NPs with varying average particle sizes

Molar ratio [CTAB]/[Fe <sub>3</sub> O <sub>4</sub> ]	Molar composition [CTAB]:[TEOS]: [NaOH]:[H <sub>2</sub> O]	Average particle diameter, <sup>a</sup> nm
12	1:4.9:1.1:5983	25
12	1:9.7:2.2:11966	35
35	1:6.5:0.7:3989	45
35	1:9.7:1.4:7977	55
47	1:5.4:0.7:3989	65
70	1:8.1:1.1:5983	75
70	1:12:1.8:9972	85
94	1:12:2.0:11218	95

<sup>a</sup>Particle diameters of Fe<sub>3</sub>O<sub>4</sub>@mSiO<sub>2</sub> were determined by TEM ( $n = 200$ ).

The longitudinal Nuclear Magnetic Resonance Dispersion (NMRD) profiles were recorded at 37 °C on a Fast Field Cycling Relaxometer (Stelar, Italy) and the longitudinal relaxivities ( $r_1$ ) were measured over a magnetic field ranging from 0.013 to 15 MHz. The inflection point appearing at high magnetic field on the NMRD curve corresponds to the condition of  $\omega_1\tau_D \approx 1$  and the determination of translational correlation time  $\tau_D$  gives the crystal size based on the equation  $\tau_D = r^2/D$ , where  $\omega_1$  is the angular frequency of the proton precession,  $D$  is the relative diffusion constant of the paramagnetic center and the solvent molecule, and  $r$  is their distance of closest approach, which determines the radius of the magnetic particle. The specific magnetization  $M_{s, \text{relaxo}}$  can be obtained from the equation  $M_{s, \text{relaxo}} \approx (R_{\text{max}}/C\tau_D)^{1/2}$ , where  $C$  is a constant and  $R_{\text{max}}$  is the maximal relaxation rate in NMRD (34). In practice, the experimental NMRD curves are fitted by the theoretical model developed in our laboratory. The relaxometric diameter and the magnetization obtained allow minimization of the least squared deviation between experimental and theoretical NMRD curves. Additional relaxivities at 20 and 60 MHz were respectively measured at 0.47 T with a Minispec PC-20 Bruker spectrometer and at 1.41 T with a Minispec Mq Series system.

## 2.4. Cell culture and determination of cell viability

OC-k3 cells were cultured at permissive conditions: 33 °C, 10% CO<sub>2</sub> in Dulbecco's modified Eagle medium (Gibco BRL, Gaithersburg, MD, USA) supplemented with 10% fetal bovine serum (Gibco BRL, Gaithersburg, MD, USA), 50 U ml<sup>-1</sup> of recombinant mouse interferon- $\gamma$  (Genzyme, Cambridge, MA, USA) and without antibiotics (35).

Cell viability was measured by flow cytometry analysis and MTS [3-(4,5-dimethylthiazol-2-yl)-5-(3-carboxymethoxyphenyl)-2-(4-sulfophenyl)-2H-tetrazolium, inner salt] assay. For flow cytometry analysis, OC-k3 cells were grown in six-well plates at a density of 150 000 cells ml<sup>-1</sup> (2 ml in each well). After cells had adhered to the plates (16–18 h), they were treated with Fe<sub>3</sub>O<sub>4</sub>-CTAB or Fe<sub>3</sub>O<sub>4</sub>@mSiO<sub>2</sub> NPs of various concentrations (ranging from Fe<sub>3</sub>O<sub>4</sub> 150 ng ml<sup>-1</sup> to 1.5  $\mu$ g ml<sup>-1</sup>) and incubated for 3–48 h. Stock solutions were prepared in physiological solution. For each experiment, two samples were prepared for each particle concentration and two samples with untreated cells. After 3 and 48 h, respectively, the cells were recovered using trypsin-EDTA solution (1 min at 37 °C), and were then processed for analysis using FACSCalibur flow cytometer (Beckman Coulter, Miami, FL, USA). The samples were collected in the appropriate tubes and 2  $\mu$ g ml<sup>-1</sup> propidium iodide (PI) was added. They were then kept in the dark and on ice for 10

min. Each sample was subjected to a test without PI (negative control or white) and one with NP40 and PI (positive control). Data were collected from at least 10 000 events.

For MTS assay, the CellTiter 96 assay (Promega, Italy) was used and OC-k3 cells were grown in 96-well plates at a density of 5000 cells ml<sup>-1</sup> (0.5 ml in each well). After cells had adhered to the plates (16–18 h), they were treated with varying particle concentrations (ranging from Fe<sub>3</sub>O<sub>4</sub> 75 ng ml<sup>-1</sup> to 15  $\mu$ g ml<sup>-1</sup>) and incubated for 3 h. Stock solutions were prepared in physiological solution. The reagent contains a tetrazolium compound MTS and an electron-coupling reagent phenazine methosulfate. MTS is bio-reduced by the dehydrogenase enzymes found in metabolically active cells into a formazan product, which is soluble in tissue culture medium. The quantity of formazan product measured at 492 nm absorbance is directly proportional to the number of living cells in culture. The reagent was added to culture wells and the cells were incubated for 2 hrs. Optical density was read at 492 nm in a microplate reader Sirio (Italy). Data are indicated as a percentage of untreated controls.

## 2.5. Statistical analyses

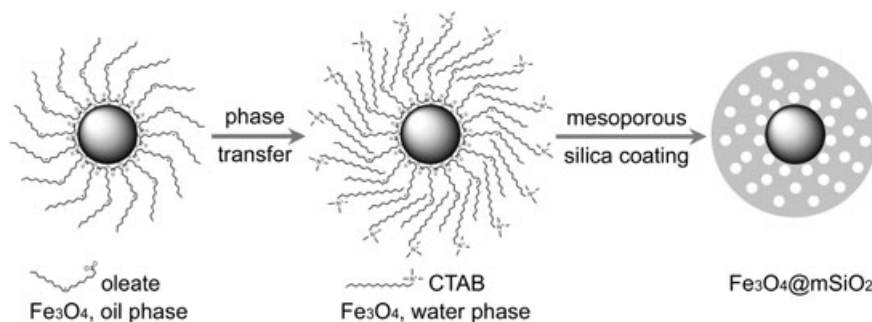
All experiments were repeated three times and the results were reproducible. All data were expressed as means  $\pm$  standard error of mean (SEM). One-way ANOVA was used to assess the differences between multiple groups. Values of  $p < 0.05$  were considered to be statistically significant.

# 3. RESULTS AND DISCUSSION

A typical procedure for the synthesis of Fe<sub>3</sub>O<sub>4</sub>@mSiO<sub>2</sub> is depicted in Scheme 1. The surfactant CTAB serves as a phase transfer agent for oleic acid-capped Fe<sub>3</sub>O<sub>4</sub> by coupling its alkyl chain to that of oleic acid through the hydrophobic van der Waals interactions, whilst the hydrophilic head group of CTAB facilitates the aqueous dispersion of Fe<sub>3</sub>O<sub>4</sub> NPs with thermodynamically defined bilayer structures (36). It is important to completely remove chloroform during the phase transfer process in order to obtain water-dispersible Fe<sub>3</sub>O<sub>4</sub>-CTAB NPs without clustering. Thereafter, CTAB acts as an organic template for growing an mSiO<sub>2</sub> layer on the Fe<sub>3</sub>O<sub>4</sub> core.

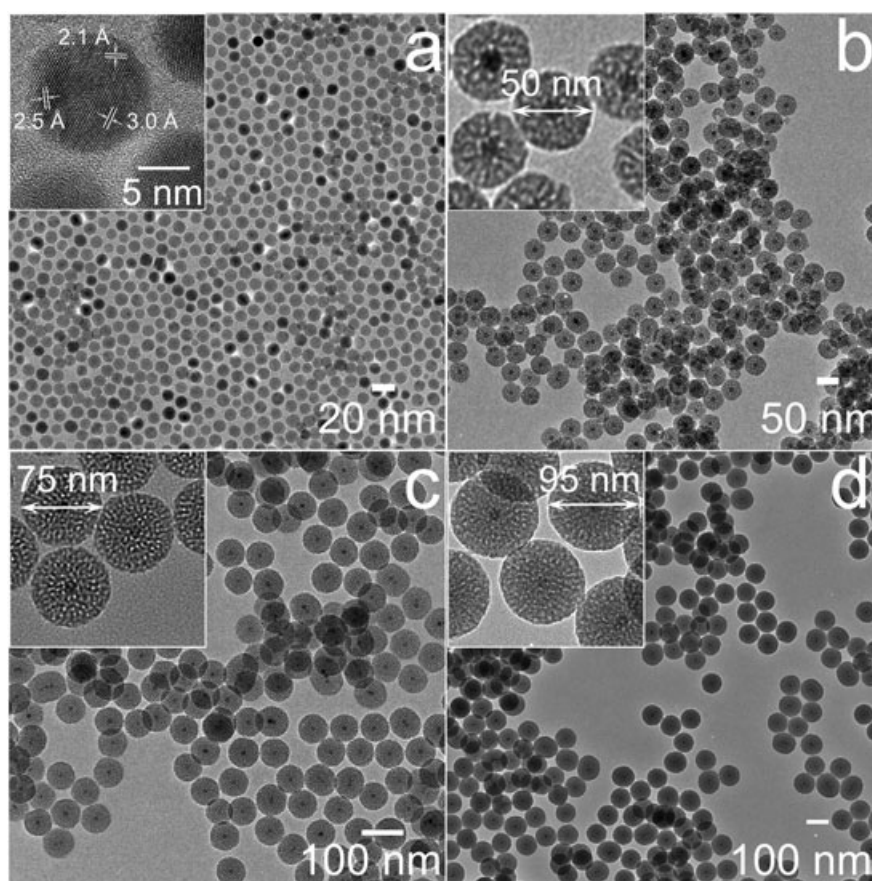
## 3.1. Morphological and structural characterization

Figure 1(a) shows the TEM micrographs of oleic acid capped Fe<sub>3</sub>O<sub>4</sub> NPs with an average diameter of 12.0 nm and a narrow size distribution (standard deviation  $\sigma \approx 5.0\%$ ). The high-resolution



**Scheme 1.** Schematic illustration of the procedure for synthesis of mesoporous silica coated iron oxide core-shell NPs.





**Figure 1.** Transmission electron microscope (TEM) micrographs of (a) hydrophobic Fe<sub>3</sub>O<sub>4</sub> NPs, and core-shell NPs of (b) 50 nm, (c) 75 nm and (d) 95 nm Fe<sub>3</sub>O<sub>4</sub>@mSiO<sub>2</sub> with the same core. The insets show the magnified images for each sample.

TEM image (inset of Fig. 1a) shows the single crystalline nature of these hydrophobic particles, and the phase-transferred Fe<sub>3</sub>O<sub>4</sub> NPs capped by CTAB remain morphologically intact (data not shown). Morphology of Fe<sub>3</sub>O<sub>4</sub>@mSiO<sub>2</sub> NPs with average diameter ranging from 25 to 95 nm are shown in Fig. 1(b–d) and Fig. S1 (in the Supporting Information). Low-magnification images show that the particles are uniform and separated from each other. High-magnification images (insets of Fig. 1b–d) show ca. 2 nm wormhole-like mesopores in the mSiO<sub>2</sub> layers of core-shell NPs. We investigated the influence of synthetic reagents on the morphology of mSiO<sub>2</sub> coatings and the optimized parameters for producing well-defined core-shell structures are summarized in Table 1. It was found that the concentration of CTAB, used for phase transfer, determines the thickness of the subsequent mSiO<sub>2</sub> coating layer. For a given amount of core materials, excess CTAB

will produce mSiO<sub>2</sub> spheres without Fe<sub>3</sub>O<sub>4</sub> cores, as by-products, owing to the presence of a large number of CTAB micelles. On the contrary, the deficiency of CTAB limits the increase in shell thickness for core-shell NPs despite the excessive amount of TEOS. If the ratios between Fe<sub>3</sub>O<sub>4</sub> and CTAB and water are optimized, where mSiO<sub>2</sub> is coated on a single magnetite core, an excess amount of TEOS will condense in the mesopores, leading to pore blockage (data not shown). To grow thicker and nonblocked mSiO<sub>2</sub> shell, the ratios of [CTAB]/[Fe<sub>3</sub>O<sub>4</sub>] and [H<sub>2</sub>O]/[CTAB] have to be increased to allow more TEOS to hydrolyze and condense around the magnetic core (see Table 1).

Figure 2 shows XRD patterns of Fe<sub>3</sub>O<sub>4</sub> and Fe<sub>3</sub>O<sub>4</sub>@mSiO<sub>2</sub>. Average crystal size of Fe<sub>3</sub>O<sub>4</sub> NPs was calculated as 11.1 nm using the Debye–Scherrer formula, which is in good agreement with the average diameter measured from TEM images,

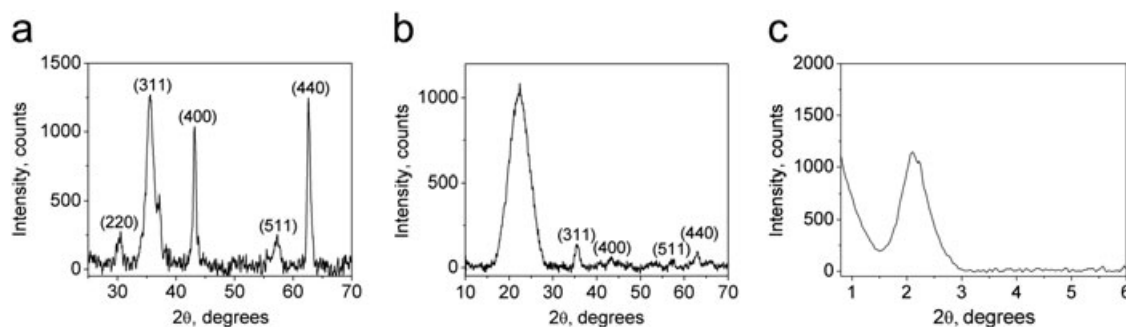


**Figure 2.** Powder X-ray diffraction (XRD) patterns of (a) Fe<sub>3</sub>O<sub>4</sub> NPs, (b) high angle and (c) low angle pattern of 75 nm Fe<sub>3</sub>O<sub>4</sub>@mSiO<sub>2</sub> NPs.

indicating that they are dominantly single crystalline. In Fig. 2(b), the broadest peak centered at  $22^\circ(2\theta)$  is consistent with the amorphous nature of the silica wall of  $\text{Fe}_3\text{O}_4@\text{mSiO}_2$  and the characteristic peaks of a magnetite structure demonstrate that the magnetic core embedded in silica shell retains its original crystalline nature. The low-angle XRD pattern of extracted  $\text{Fe}_3\text{O}_4@\text{mSiO}_2$  (Fig. 2c) exhibits only one diffraction peak (unit cell parameter ca. 30 Å) and the absence of high-order reflections reveals the reduction in the long-range mesoscale order, which might be due to the interference of magnetic core in the structure of  $\text{mSiO}_2$ . The corresponding mesoporous material, Mobile Crystalline Material-41 (MCM-41), synthesized using CTAB without  $\text{Fe}_3\text{O}_4$  cores, shows a two-dimensional hexagonal porous structure (Fig. S2a and b).

$\text{N}_2$  adsorption/desorption isotherms of  $\text{Fe}_3\text{O}_4@\text{mSiO}_2$  (Fig. 3) exhibit a characteristic type IV isotherm as expected for  $\text{mSiO}_2$  material. The BET surface area and the total pore volume of extracted 75 nm  $\text{Fe}_3\text{O}_4@\text{mSiO}_2$  NPs are  $202 \text{ m}^2 \text{ g}^{-1}$  and  $0.29 \text{ cm}^3 \text{ g}^{-1}$ , respectively. The corresponding PSD calculated using NLDFT model (inset of Fig. 3) demonstrates a bimodal porosity (pore size 14 and 27 Å). Compared with the corresponding MCM-41 particles, which show a single modal PSD (pore size 31 Å, Fig. S2d), the bimodal PSD of  $\text{Fe}_3\text{O}_4@\text{mSiO}_2$  NPs might be induced by the heterogeneous growth of  $\text{mSiO}_2$  layer on  $\text{Fe}_3\text{O}_4$  NP cores and hence a broad distribution of pore size.

### 3.2. Magnetic and relaxometric characterization

Field-dependent magnetization of  $\text{Fe}_3\text{O}_4$ -CTAB and  $\text{Fe}_3\text{O}_4@\text{mSiO}_2$  NPs with different shell thicknesses was examined at room temperature using VSM. None of the suspensions showed a hysteresis (Fig. 4), demonstrating that they are super-paramagnetic, which is a desirable characteristic for  $T_2$  MRI contrast agents. The saturation magnetizations ( $M_s$ ) of  $\text{Fe}_3\text{O}_4$ -CTAB, and 50 and 75 nm  $\text{Fe}_3\text{O}_4@\text{mSiO}_2$  NPs are 48.7, 48.3 and  $47.1 \text{ A m}^2 \text{ kg}^{-1} \text{ Fe}$ , respectively. By fitting the magnetization data to Langevin equation (37), magnetic domain sizes of the magnetic cores of these samples were calculated as 11.7, 11.8 and 11.8 nm respectively, which are close to the values obtained using TEM and XRD. Results of relaxivity measurements ( $r_1$  and  $r_2$ ) and hydrodynamic

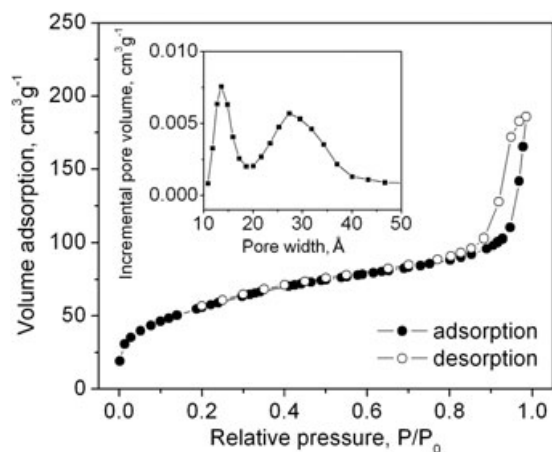


**Figure 3.**  $\text{N}_2$  adsorption (solid)-desorption (hollow) isotherms (inset: nonlocal density functional theory slit-type model for pore size distribution from adsorption branch) of 75 nm  $\text{Fe}_3\text{O}_4@\text{mSiO}_2$  NPs with surfactant extracted and oven-dried at  $80^\circ \text{C}$ .

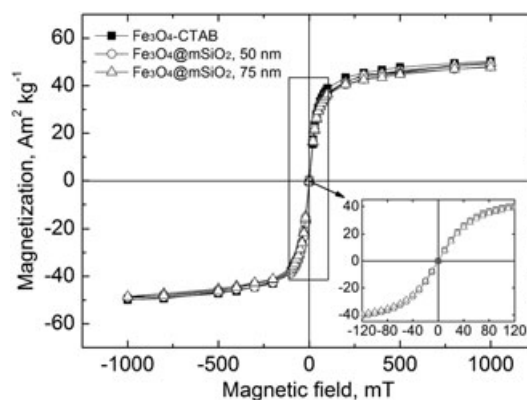


**Figure 4.** Field-dependent magnetization measurement of aqueous suspensions of  $\text{Fe}_3\text{O}_4$ -CTAB and  $\text{Fe}_3\text{O}_4@\text{mSiO}_2$  NPs (50 and 75 nm, respectively) at room temperature normalized for Fe content; the inset represents enlarged part of magnetization curve.

sizes of  $\text{Fe}_3\text{O}_4$ -CTAB and  $\text{Fe}_3\text{O}_4@\text{mSiO}_2$  NPs with various coating thicknesses are summarized in Table 2. The  $r_2$  value of  $\text{Fe}_3\text{O}_4$ -CTAB is similar to those of  $\text{Fe}_3\text{O}_4@\text{mSiO}_2$  NPs. However, the value of  $r_1$  is one order of magnitude higher than those of  $\text{Fe}_3\text{O}_4@\text{mSiO}_2$  NPs. Since the effect of surface chemistry on relaxivity most likely arises from the hydrophilicity of the coating layers and the coordination between the inner capping ligands, both influencing spin disorders (28), the big difference in the values of  $r_1$  is proposed to be due to the different effects between CTAB and  $\text{mSiO}_2$  coating layers on the mobility of water molecules. For  $\text{Fe}_3\text{O}_4@\text{mSiO}_2$  NPs with varying coating thickness, it was found that the values of  $r_1$  are effectively decreased by ca. 6 times (at 20 MHz) and ca. 4.5 times (at 60 MHz) when particle size increased from 50 to 95 nm, whilst  $r_2$  decreased by only ca. 40% at 20 and 60 MHz. The magnitude of  $r_1$  has been reported to be dependent on the magnetization of the material, the electron spin relaxation time and the accessibility of protons bearing nuclear spins to the surface of iron oxide (39). The decreased value of  $r_1$  for  $\text{Fe}_3\text{O}_4@\text{mSiO}_2$  with increased silica shell thickness may reflect the ability of  $\text{mSiO}_2$  coatings on separating water from the surface of the magnetite NPs (5). Similar studies on the effect of polymeric coating on relaxivities also showed that the hydrophilicity of the coating layer has a positive effect on enhancing the proton relaxivities (both  $r_1$  and  $r_2$ ) for  $\text{Fe}_3\text{O}_4$  particles (28). Superparamagnetic contrast agents are known to be able to produce a long-range magnetic field to promote the spin-spin relaxation process of surrounding water molecules (4), and the magnitude of  $r_2$  is believed to reflect the ability of the magnetic material to produce local inhomogeneity in the magnetic field (40). Our results suggest that the locally generated magnetic field by  $\text{Fe}_3\text{O}_4$  cores has been weakened moderately by the increased thickness of  $\text{mSiO}_2$  coating.

Owing to  $\text{mSiO}_2$  coatings, the extent of decrease of  $r_1$  is more than that of  $r_2$ , and the  $r_2/r_1$  ratio increases as a function of the coating thickness, which is 82.2 at 20 MHz and 179 at 60 MHz for 95 nm  $\text{Fe}_3\text{O}_4@\text{mSiO}_2$  (see Table 2). The great enhancement of  $r_2/r_1$  ratio, ca. 21 and ca. 14 times higher than that of the two commercial iron oxide-based contrast agents (see Table 2), indicates a high efficiency of  $\text{Fe}_3\text{O}_4@\text{mSiO}_2$  on  $T_2$  MR imaging. In comparison, previous reports on relaxivity of conventional amorphous  $\text{SiO}_2$ -coated  $\text{Fe}_3\text{O}_4$  ( $\text{Fe}_3\text{O}_4@\text{aSiO}_2$ ) showed no clear

**Table 2.** Mean hydrodynamic diameters and relaxivities of Fe<sub>3</sub>O<sub>4</sub>-CTAB and different sized Fe<sub>3</sub>O<sub>4</sub>@mSiO<sub>2</sub> NPs measured at 20 MHz (0.47 T) and 60 MHz (1.41 T) in water (37 °C), and the reported relaxivity values for commercial Feridex<sup>®</sup> and Resovist<sup>®</sup> contrast agents

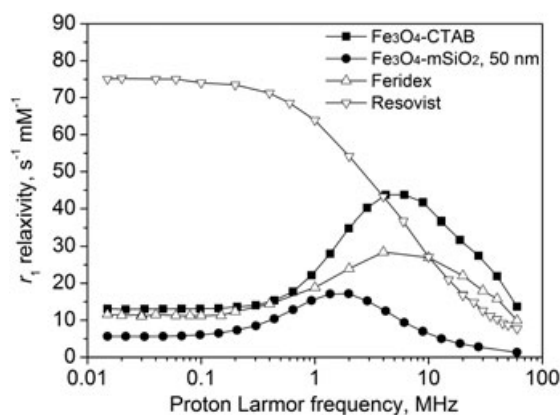
Sample name (particle diameter by TEM)	Mean hydrodynamic diameter (nm) <sup>a</sup>	20 MHz			60 MHz		
		<i>r</i> <sub>1</sub>	<i>r</i> <sub>2</sub>	<i>r</i> <sub>2</sub> / <i>r</i> <sub>1</sub>	<i>r</i> <sub>1</sub>	<i>r</i> <sub>2</sub>	<i>r</i> <sub>2</sub> / <i>r</i> <sub>1</sub>
		(s <sup>-1</sup> mM <sup>-1</sup> )	(s <sup>-1</sup> mM <sup>-1</sup> )		(s <sup>-1</sup> mM <sup>-1</sup> )	(s <sup>-1</sup> mM <sup>-1</sup> )	
Fe <sub>3</sub> O <sub>4</sub> -CTAB (11 nm)	67	31.25	81.37	2.61	13.69	82.18	6.01
Fe <sub>3</sub> O <sub>4</sub> @mSiO <sub>2</sub> (50 nm)	60	3.65	84.26	23.1	1.31	92.13	70.3
Fe <sub>3</sub> O <sub>4</sub> @mSiO <sub>2</sub> (75 nm)	77	2.13	79.93	37.5	0.97	87.54	90.3
Fe <sub>3</sub> O <sub>4</sub> @mSiO <sub>2</sub> (95 nm)	96	0.61	50.13	82.2	0.31	55.44	179
Feridex (5)	72	40	160	4	—	—	—
Resovist (38)	65	25	164	6.2	—	—	—

<sup>a</sup>Mean value based on volume distribution.

trend of enhancement (41) for *r*<sub>2</sub>/*r*<sub>1</sub> ratios or even decreased values (31) were found with the increases in coating thicknesses. The different effects between aSiO<sub>2</sub> and mSiO<sub>2</sub> coatings on enhancement of *r*<sub>2</sub>/*r*<sub>1</sub> ratios, crucial for *T*<sub>2</sub> MRI efficiency, are most probably due to the different influences of their structures on the hydrophilicity and inhomogeneity of the local magnetic field.

Nuclear magnetic resonance (NMR) relaxometry plays an important role in evaluating the properties of superparamagnetic colloids as potential contrast agents (42). The effects of surface coatings on the relaxometric property of SPIONs are examined and compared between CTAB-coated and mSiO<sub>2</sub>-coated Fe<sub>3</sub>O<sub>4</sub> NPs using NMR relaxometry. Figure 5 shows NMRD profiles of Fe<sub>3</sub>O<sub>4</sub>-CTAB, Fe<sub>3</sub>O<sub>4</sub>@mSiO<sub>2</sub> NPs, and two commercial MRI contrast agents, which represent the longitudinal relaxivity *r*<sub>1</sub> as a function of the external magnetic field. The relaxometric data can be related to the morphological and physical properties of magnetic particles via previously proposed proton relaxivity theories, namely Freed's equation, Ayant's equation or a sum of the two weighted by the squared Langevin function (43). Table 3 summarizes the average diameters and magnetization values of Fe<sub>3</sub>O<sub>4</sub>-CTAB and Fe<sub>3</sub>O<sub>4</sub>@mSiO<sub>2</sub> NPs obtained by fitting NMRD profiles and by magnetometric measurement, respectively. Relaxometry of Fe<sub>3</sub>O<sub>4</sub>-CTAB NPs provides the average magnetic core size as 12.5 nm and specific magnetization as 48.2 A m<sup>2</sup> kg<sup>-1</sup> Fe, which are close to the results of magnetic domain size and magnetization measured by magnetometry and indicate the monodispersity of

these NPs. For 50 nm Fe<sub>3</sub>O<sub>4</sub>@mSiO<sub>2</sub>, the diameter of the magnetite core embedded in mSiO<sub>2</sub> was calculated as 28 nm and the specific magnetization as 14.3 A m<sup>2</sup> kg<sup>-1</sup> Fe by NMRD, which are very different from the results obtained by magnetometry. Previous studies showed that the crystal size distribution (44) or cluster morphology (45) is responsible for the differences between relaxometric and magnetometric results. In the present study, since the particles are uniform and well dispersed, we ascribe these differences to the effect of mSiO<sub>2</sub> on diffusive permeability of water molecules. This is because the determination of magnetic crystal radius *r* and specific magnetization *M*<sub>s</sub> by NMRD is closely related to diffusion parameters (e.g., *τ*<sub>D</sub> and *D*) (34,46). We therefore propose that, when the coating is permeable to water molecules, i.e. for Fe<sub>3</sub>O<sub>4</sub>-CTAB NPs, magnetometry and relaxometry result in similar results for the diameter of the magnetic cores and magnetization. On the contrary, when the coating is completely impermeable, the magnetic core size measured by relaxometry should exhibit the same value as hydrodynamic size of the core-shell particles. The magnetic core size of 50 nm Fe<sub>3</sub>O<sub>4</sub>@mSiO<sub>2</sub> NPs obtained by relaxometry was 28 nm (see Table 3), an intermediate value between that measured by magnetometry and the hydrodynamic size of core-shell NPs. This demonstrates that the mSiO<sub>2</sub> coating is partially permeable and the water molecules seeping across the coating are highly constrained in its spread. Therefore, the *r*<sub>1</sub> of Fe<sub>3</sub>O<sub>4</sub>@mSiO<sub>2</sub> is much lower than that of Fe<sub>3</sub>O<sub>4</sub>-CTAB NPs.

**Figure 5.** NMRD profiles of Fe<sub>3</sub>O<sub>4</sub>-CTAB, 50 nm Fe<sub>3</sub>O<sub>4</sub>@mSiO<sub>2</sub> NPs, and Feridex<sup>®</sup> and Resovist<sup>®</sup> recorded at 37 °C.

### 3.3. Cell viability assessment

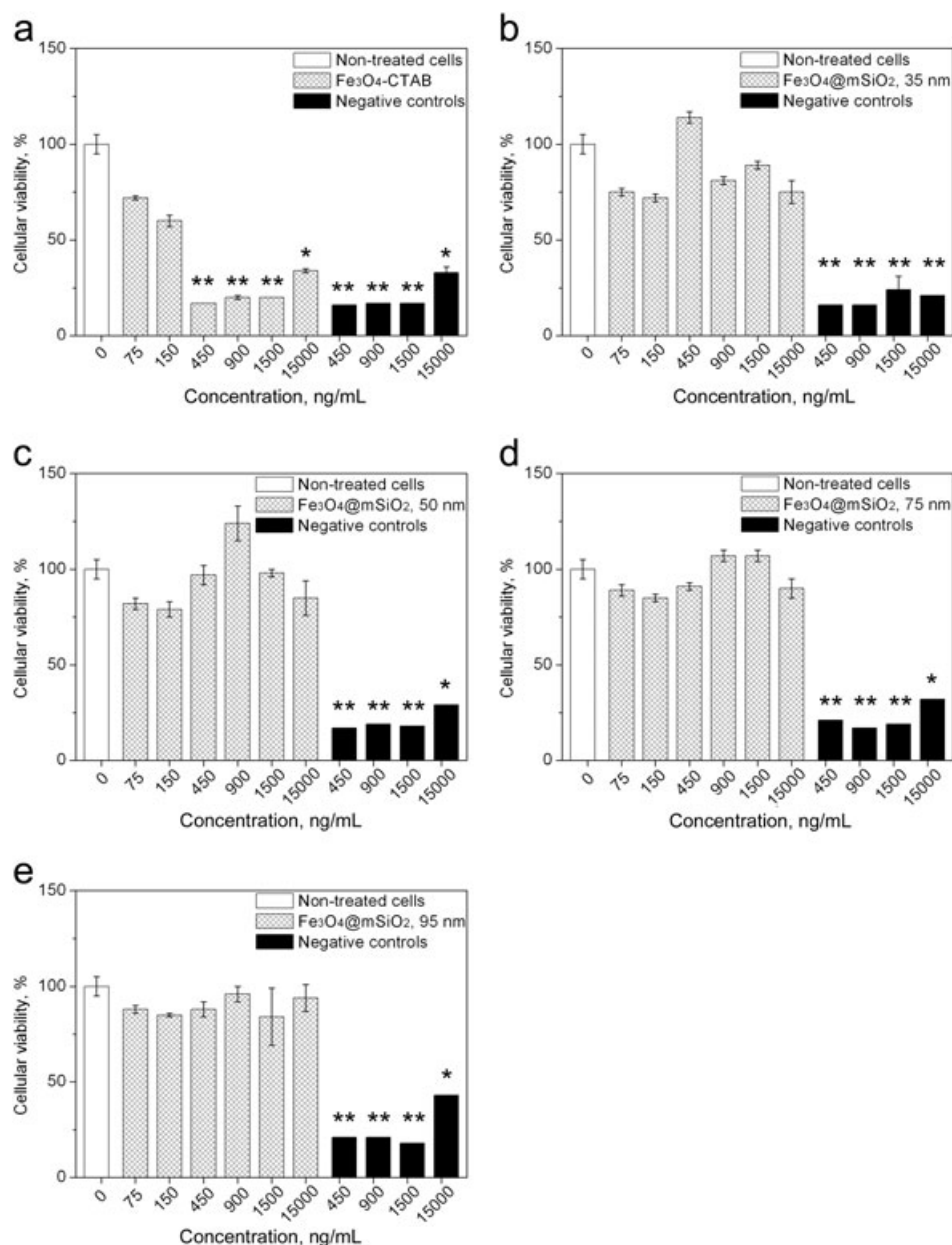
In order to study the effect of engineered NPs on the viability of OC-k3 cells [epithelial cells derived from the organ of Corti of transgenic mouse (47)], the cells were incubated with different particle concentrations for 3 h and their viability was measured by MTS assay. The Fe<sub>3</sub>O<sub>4</sub>-CTAB NPs induced decreases in MTS levels at 75 and 150 ng ml<sup>-1</sup> and showed high toxicity at higher doses (highly significant, *p* < 0.001; Fig. 6a). The treatments with varying sized Fe<sub>3</sub>O<sub>4</sub>@mSiO<sub>2</sub> NPs (35–95 nm) did not induce considerable toxic effects and the mortality rate was not significantly different from that of the untreated cells (Fig. 6b–e; data confirmed also by flow cytometry analysis). After a 48 h incubation period, Fe<sub>3</sub>O<sub>4</sub>-CTAB NPs produced significant toxicity level at all the doses tested, while the Fe<sub>3</sub>O<sub>4</sub>@mSiO<sub>2</sub> NPs had no major negative impact on cell viability (see Fig. 7).

Fe<sub>3</sub>O<sub>4</sub>-CTAB NPs show toxicity in the performed test and we observed the L50 proteins between the Fe<sub>3</sub>O<sub>4</sub> doses of 75–150



**Table 3.** Summary of magnetic crystal diameter ( $D_{\text{relaxo}}$  and  $D_{\text{magneto}}$ ) and magnetization ( $M_{\text{s relaxo}}$  and  $M_{\text{s magneto}}$ ) of  $\text{Fe}_3\text{O}_4$ -CTAB and  $\text{Fe}_3\text{O}_4$ @mSiO<sub>2</sub> NPs obtained by relaxometry and magnetometry, respectively; crystal diameter and magnetization of Feridex<sup>®</sup> and Resovist<sup>®</sup> measured by relaxometry

Sample name	$D_{\text{relaxo}}$ (nm)	$D_{\text{magneto}}$ (nm)	$M_{\text{s relaxo}}$ (A m <sup>2</sup> kg <sup>-1</sup> Fe)	$M_{\text{s magneto}}$ (A m <sup>2</sup> kg <sup>-1</sup> Fe)
$\text{Fe}_3\text{O}_4$ -CTAB	12.5	11.7	48.2	48.7
$\text{Fe}_3\text{O}_4$ @mSiO <sub>2</sub>	28	11.8	14.3	48.3
Feridex	6.7	—	38.3	—
Resovist	17.0	—	38.0	—

**Figure 6.** The dose-response relationships of the *in vitro* systems exposed for 3 h with (a)  $\text{Fe}_3\text{O}_4$ -CTAB NPs, (b–e) 35, 50, 75 and 95 nm  $\text{Fe}_3\text{O}_4$ @mSiO<sub>2</sub> NPs. Cellular viability is measured in MTS activity (absorbance at 492 nm) over an increasing concentration range from 75 to 15 000 ng ml<sup>-1</sup>. The values are the means of three experiments with the error bar indicating SEM. \*\* $p < 0.001$ ; \* $p < 0.05$ , when compared with nontreated cell viability value (Bonferroni, ANOVA).

ng ml<sup>-1</sup> until 3 h exposure. A previous report showed that  $\gamma$ -Fe<sub>2</sub>O<sub>3</sub> particles became drastically toxic after 48 h of exposure through oxidative stress (48); however, we observed that the

$\text{Fe}_3\text{O}_4$ @mSiO<sub>2</sub> NPs did not reveal any significant toxicity after this period of time. Although the mechanism underlying NP-induced cytotoxicity is not completely understood, the cytotoxicity of

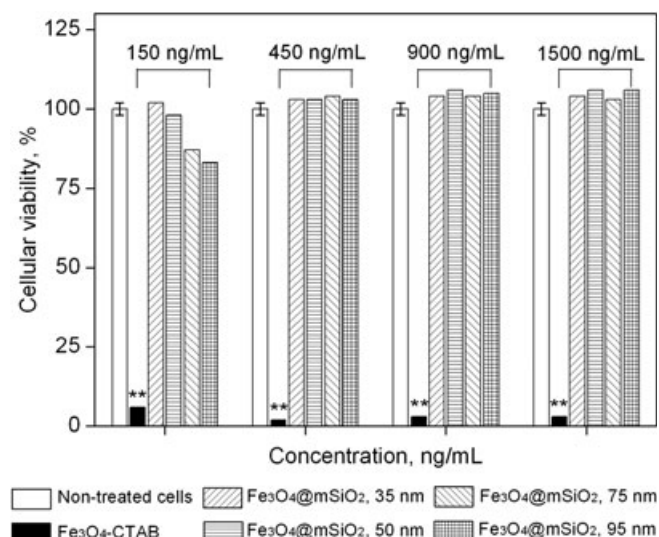


**Figure 7.** Flow cytometry data showing percentage cellular viability after 48 h incubation with various concentrations of NPs. The values are the means of three experiments with the error bar indicating SEM. \*\*  $p < 0.001$ , when compared with nontreated cell viability value (Bonferroni, ANOVA).

Fe<sub>3</sub>O<sub>4</sub>-CTAB NPs could be associated with three factors: the oxidant effect of the iron core, the CTAB release and the NP dimension. Earlier work indicates that the cytotoxicity of iron particles could be due to reactive oxygen species (ROS) induction (49). Wei *et al.* demonstrated that Fe<sub>3</sub>O<sub>4</sub> coated with different materials are toxic in a dose-dependent manner, with an LD50 of about 500 ng ml<sup>-1</sup> (50). Furthermore it is well documented that high concentrations of CTAB are not biocompatible (51,52), thus we cannot exclude a toxic effect of the CTAB coating of the Fe<sub>3</sub>O<sub>4</sub> particles. For various sized Fe<sub>3</sub>O<sub>4</sub>@mSiO<sub>2</sub> NPs, no severe time- or dose-dependent toxicity was observed, which is desirable for further MRI measurements.

## 4. CONCLUSIONS

In summary, we have performed an in-depth study of the effects of surface coating on relaxivities of iron oxide particles for MRI. Tunable relaxivities were obtained by varying the thickness of the mSiO<sub>2</sub> coating layer of Fe<sub>3</sub>O<sub>4</sub>@mSiO<sub>2</sub> NPs. It was found that  $r_1$  shows a dramatic decrease accompanied by a smaller decrease in  $r_2$ , with an increase in mSiO<sub>2</sub> coating thickness. Consequently, Fe<sub>3</sub>O<sub>4</sub>@mSiO<sub>2</sub> NPs exhibit enhanced MRI efficiency, which is ca. 21 times higher than that of the commercial T<sub>2</sub> contrast agents. NMR relaxometry studies provide the proof that the mSiO<sub>2</sub> layer is partially permeable to water molecules, which accounts for the decrease in  $r_1$  and enhancement of the  $r_2/r_1$  ratio. Biocompatibility studies show that Fe<sub>3</sub>O<sub>4</sub>@mSiO<sub>2</sub> NPs have no negative impact on cell viability, which supports the potential application of these particles as a highly efficient and biocompatible MRI T<sub>2</sub> contrast agent.

## Supporting Information

Supporting information may be found in the online version of this paper.

## Acknowledgments

This work has been partially supported by European Commission FP6-funded NanoEar (NMP4-CT-2006-026556) and FP7-funded NanoMune (NMP4-SL-2008-214281) projects, the Fonds de la Recherche Scientifique, the ARC Program 05/10-335 of the French Community of Belgium and the ENCITE program of the European Community. The support and sponsorship concerted by COST Action D38 'Metal-based systems for Molecular Imaging Applications' and the EMIL program are kindly acknowledged. Thanks go to Dr Alfonso E. Garcia-Bennett and Dr Rambabu Atluri (Nanotechnology and Functional Materials, Ångström Laboratory, Uppsala University, Sweden) for technical support for N<sub>2</sub> adsorption/desorption isotherms measurement.

## REFERENCES

- Geraldes CFGC, Laurent S. Classification and basic properties of contrast agents for magnetic resonance imaging. *Contrast Media Mol Imag* 2009; 4: 1–23.
- Na HB, Song IC, Hyeon T. Inorganic nanoparticles for MRI contrast agents. *Adv Mater* 2009; 21: 2133–2148.
- Poe D, Zou J, Zhang W, Qin J, Ramadan UA, Fornara A, Muhammed M, Pyykkö I. MRI of the cochlea with superparamagnetic iron oxide nanoparticles compared to gadolinium chelate contrast agents in a rat model. *Eur J Nanomed* 2009; 2: 29–36.
- McRobbie DW, Moore EA, Graves MJ, Prince MR. *MRI from Picture to Proton*. Cambridge University Press: Cambridge, 2006.
- Josephson L, Lewis J, Jacobs P, Hahn PF, Stark DD. The effects of iron oxides on proton relaxivity. *Magn Reson Imag* 1988; 6: 647–653.
- Jun Y-W, Lee J-H, Cheon J. Chemical design of nanoparticle probes for high-performance magnetic resonance imaging. *Angew Chem Int Ed* 2008; 47: 5122–5135.
- Yu MK, Jeong YY, Park J, Park S, Kim JW, Min JJ, Kim K, Jon S. Drug-loaded superparamagnetic iron oxide nanoparticles for combined cancer imaging and therapy in vivo. *Angew Chem Int Ed* 2008; 47: 5362–5365.
- Lee N, Kim H, Choi SH, Park M, Kim D, Kim H-C, Choi Y, Lin S, Kim BH, Jung HS, Kim H, Park KS, Moon WK, Hyeon T. Magnetosome-like ferrimagnetic iron oxide nanocubes for highly sensitive MRI of single cells and transplanted pancreatic islets. *Proc Natl Acad Sci USA* 2011; 108: 2662–2667.
- Ohgushi M, Nagayama K, Wada A. Dextran-magnetite: a new relaxation reagent and its application to T<sub>2</sub> measurements in gel systems. *J Magn Res* 1978; 29: 599–601.
- Kandori K, Fukuoka M, Ishikawa T. Effects of citrate ions on the formation of ferric oxide hydroxide particles. *J Mater Sci* 1991; 26: 3313–3319.
- Ma M, Zhang Y, Yu W, Shen H-Y, Zhang H-Q, Gu N. Preparation and characterization of magnetite nanoparticles coated by amino silane. *Colloids Surf, A* 2003; 212: 219–226.
- Sun S, Zeng H, Robinson DB, Raoux S, Rice PM, Wang SX, Li G. Monodisperse MFe<sub>2</sub>O<sub>4</sub> (M = Fe, Co, Mn) nanoparticles. *J Am Chem Soc* 2004; 126: 273–279.
- Park J, An K, Hwang Y, Park J-G, Noh H-J, Kim J-Y, Park J-H, Hwang N-M, Hyeon T. Ultra-large-scale syntheses of monodisperse nanocrystals. *Nat Mater* 2004; 3: 891–895.
- Jun Y-W, Huh Y-M, Choi J-S, Lee J-H, Song H-T, Kim S, Kim S, Yoon S, Kim K-S, Shin J-S, Suh J-S, Cheon J. Nanoscale size effect of magnetic nanocrystals and their utilization for cancer diagnosis via magnetic resonance imaging. *J Am Chem Soc* 2005; 127: 5732–5733.
- Qin J, Laurent S, Jo YS, Roch A, Mikhaylova M, Bhujwala ZM, Muller RN, Muhammed M. A high-performance magnetic resonance imaging T<sub>2</sub> contrast agent. *Adv Mater* 2007; 19: 1874–1878.
- Casula MF, Floris P, Innocenti C, Lascialfari A, Marinone M, Corti M, Sperling RA, Parak WJ, Sangregorio C. Magnetic resonance imaging contrast agents based on iron oxide superparamagnetic ferrofluids. *Chem Mater* 2010; 22: 1739–1748.
- Kim J, Kim HS, Lee N, Kim T, Kim H, Yu T, Song IC, Moon WK, Hyeon T. Multifunctional uniform nanoparticles composed of a magnetite nanocrystal core and a mesoporous silica shell for magnetic



- resonance and fluorescence imaging and for drug delivery. *Angew Chem Int Ed* 2008; 47: 8438–8441.
18. Gorelikov I, Matsuura N. Single-step coating of mesoporous silica on cetyltrimethyl ammonium bromide-capped nanoparticles. *Nano Lett* 2008; 8: 369–373.
  19. Hu X, Zrazhevskiy P, Gao X. Encapsulation of single quantum dots with mesoporous silica. *Ann Biomed Eng* 2009; 37: 1960–1966.
  20. Vallet-Regí M, Balas F, Arcos D. Mesoporous materials for drug delivery. *Angew Chem Int Ed* 2007; 46: 7548–7558.
  21. Rosenholm JM, Sahlgren C, Lindén M. Multifunctional mesoporous silica nanoparticles for combined therapeutic, diagnostic and targeted action in cancer treatment. *Curr Drug Targets* 2011; 12: 1166–1186.
  22. Yiu HHP, Niu H-J, Biermans E, Tendeloo GV, Rosseinsky MJ. Designed multifunctional nanocomposites for biomedical applications. *Adv Funct Mater* 2010; 20: 1599–1609.
  23. Drummond DC, Meyer O, Hong K, Kirpotin DB, Papahadjopoulos D. Optimizing liposomes for delivery of chemotherapeutic agents to solid tumors. *Pharmacol Rev* 1999; 51: 691–744.
  24. Lee DY. Highly effective T<sub>2</sub> MR contrast agent based on heparinized superparamagnetic iron oxide nanoparticles. *Macromol Res* 2011; 19: 843–847.
  25. Reimer P, Tombach B. Hepatic MRI with SPIO: detection and characterization of focal liver lesions. *Eur Radiol* 1998; 8: 1198–1204.
  26. Lartigue L, Innocenti C, Kalaivani T, Awwad A, Duque MMS, Guari Y, Larionova J, Guérin C, Montero JLG, Barragan-Montero V, Arosio P, Lascialfari A, Gatteschi D, Sangregorio C. Water-dispersible sugar-coated iron oxide nanoparticles. An evaluation of their relaxometric and magnetic hyperthermia properties. *J Am Chem Soc* 2011; 133: 10459–10472.
  27. LaConte LEW, Nitin N, Zurkiya O, Caruntu D, O'Connor CJ, Hu X, Bao G. Coating thickness of magnetic iron oxide nanoparticles affects R<sub>2</sub> relaxivity. *J Magn Reson Imag* 2007; 26: 1634–1641.
  28. Duan H, Kuang M, Wang X, Wang YA, Mao H, Nie S. Reexamining the effects of particle size and surface chemistry on the magnetic properties of iron oxide nanocrystals: new insights into spin disorder and proton relaxivity. *J Phys Chem C* 2008; 112: 8127–8131.
  29. Fornara A, Recalenda A, Qin J, Sugunan A, Ye F, Laurent S, Muller RN, Zou J, Abo-Ramadan U, Toprak MS, Muhammed M. Polymeric/inorganic multifunctional nanoparticles for simultaneous drug delivery and visualization. *Mater Res Soc Symp Proc* 2010; 1257: 1257-004-03.
  30. Zhang C, Wängler B, Morgenstern B, Zentgraf H, Eisenhut M, Untenecker H, Krüger R, Huss R, Seliger C, Semmler W, Kiessling F. Silica- and alkoxy-silane-coated ultrasmall superparamagnetic iron oxide particles: a promising tool to label cells for magnetic resonance imaging. *Langmuir* 2007; 23: 1427–1434.
  31. Pinho SLC, Pereira GA, Voisin P, Kassem J, Bouchaud V, Etienne L, Peters JA, Carlos L, Mornet S, Galdes CFGC, Rocha J, Delville M-H. Fine tuning of the relaxometry of  $\gamma$ -Fe<sub>2</sub>O<sub>3</sub>@SiO<sub>2</sub> nanoparticles by tweaking the silica coating thickness. *ACS Nano* 2010; 4: 5339–5349.
  32. Astolfi L, Simoni E, Ciorba A, Martini A. In vitro protective effects of Ginkgo biloba against cisplatin toxicity in mouse cell line OCK3. *Audiol Med* 2008; 6: 251–258.
  33. Lang N, Tuel A. A fast and efficient ion-exchange procedure to remove surfactant molecules from MCM-41 materials. *Chem Mater* 2004; 16: 1961–1966.
  34. Muller RN, Elst LV, Roch A, Peters JA, Csajbok E, Gillis P, Gossuin Y. Relaxation by metal-containing nanosystems. *Adv Inorg Chem* 2005; 57: 239–292.
  35. Kalinec F, Kalinec G, Boukhvalova M, Kachar B. Establishment and characterization of conditionally immortalized organ of corti cell lines. *Cell Biol Int* 1999; 23: 175–184.
  36. Fan H, Wright A, Gabaldon J, Rodriguez A, Brinker CJ, Jiang Y-B. Three-dimensionally ordered gold nanocrystal/silica superlattice thin films synthesized via sol-gel self-assembly. *Adv Funct Mater* 2006; 16: 891–895.
  37. Bean CP, Livingston JD. Superparamagnetism. *J Appl Phys* 1959; 30: 1205–1295.
  38. Allkemper T, Bremer C, Matuszewski L, Ebert W, Reimer P. Contrast-enhanced blood-pool MR angiography with optimized iron oxides: effect of size and dose on vascular contrast enhancement in rabbits. *Radiology* 2002; 223: 432–438.
  39. Engelstad BE, Wolf GL. Contrast agents. In: *Magnetic Resonance Imaging*, Stark DD, Bradley WG (eds). Mosby: St Louis, MO, 1988.
  40. Medonca DMH, Lauterbur PC. Ferromagnetic particles as contrast agents for magnetic resonance imaging of liver and spleen. *Magn Reson Med* 1986; 3: 328–330.
  41. Kunzmann A, Andersson B, Vogt C, Feliu N, Ye F, Gabrielsson S, Toprak MS, Buerki-Thurnherr T, Laurent S, Vahter M, Krug H, Muhammed M, Scheynius A, Fadeel B. Efficient internalization of silica-coated iron oxide nanoparticles of different sizes by primary human macrophages and dendritic cells. *Toxicol Appl Pharmacol* 2011; 253: 81–93.
  42. Muller RN, Vallet P, Maton F, Roch A, Goudemant JF, Vander Elst L, Gillis P, Peto S, Moyny F, Van Haverbeke Y. Recent developments in design, characterization, and understanding of MRI and MRS contrast media. *Invest Radiol* 1990; 25: S34–S36.
  43. Laurent S, Forge D, Port M, Roch A, Robic C, Elst LV, Muller RN. Magnetic iron oxide nanoparticles: synthesis, stabilization, vectorization, physicochemical characterizations, and biological applications. *Chem Rev* 2008; 108: 2064–2110.
  44. Ouakssim A, Fastrez S, Roch A, Laurent S, Gossuin Y, Piérart C, Elst LV, Muller RN. Control of the synthesis of magnetic fluids by relaxometry and magnetometry. *J Magn Magn Mater* 2004; 272–276: e1711–e1713.
  45. Gossuin Y, Disch S, Vuong QL, Gillis P, Hermann RP, Park J-H, Sailor MJ. NMR relaxation and magnetic properties of superparamagnetic nanoworms. *Contrast Media Mol Imag* 2010; 5: 318–322.
  46. Koenig SH, Ahkong QF, Brown RD, III, Lafleur M, Spiller M, Unger E, Tilcock C. Permeability of liposomal membranes to water: results from the magnetic field dependence of T<sub>1</sub> of solvent protons in suspensions of vesicles with entrapped paramagnetic ions. *Magn Reson Med* 1992; 23: 275–286.
  47. Kalinec F, Kalinec G, Boukhvalova M, Kachar B. Establishment and characterization of conditionally immortalized organ of corti cell lines. *Cell Biol Int* 1999; 23: 175–184.
  48. Hanini A, Schmitt A, Kacem K, Chau F, Ammar S, Gavard J. Evaluation of iron oxide nanoparticle biocompatibility. *Int J Nanomed* 2011; 6: 787–794.
  49. Naqvi S, Samim M, Abidin MZ, Ahmed FJ, Maitra AN, Prashant CK, Dinda AK. Concentration-dependent toxicity of iron oxide nanoparticles mediated by increased oxidative stress. *Int J Nanomed* 2010; 5: 983–989.
  50. Wei K, Xu X, Pu X, Hou Z, Zhang Q. Cytotoxic effects and the mechanism of three types of magnetic nanoparticles on human hepatoma BEL-7402 cells. *Nanoscale Res Lett* 2011; 6: 480.
  51. Ye F, Vallhov H, Qin J, Daskalaki E, Sugunan A, Toprak MS, Fornara A, Gabrielsson S, Scheynius A, Muhammed M. Synthesis of high aspect ratio gold nanorods and their effects on human antigen presenting dendritic cells. *Int J Nanotechnol* 2011; 8: 631–652.
  52. Leonov AP, Zheng J, Clogston JD, Stern ST, Patri AK, Wei A. Detoxification of gold nanorods by treatment with polystyrenesulfonate. *ACS Nano* 2008; 2: 2481–2488.